



Doppler lidar at Observatoire de Haute Provence for wind profiling up to 75 km altitude: performance evaluation and observations

Sergey M. Khaykin¹, Alain Hauchecorne¹, Robin Wing¹, Philippe Keckhut¹, Sophie Godin-Beekmann¹, Jacques Porteneuve¹, Jean-Francois Mariscal¹, Jerome Schmitt²

- 5 1 LATMOS/IPSL, UVSQ, Sorbonne Université, CNRS, Guyancourt, France
2 Observatoire de Haute-Provence, Université d'Aix-Marseille, CNRS, Saint-Michel l'Observatoire, France

Correspondence to: Sergey Khaykin (sergey.khaykin@latmos.ipsl.fr)

10 **Abstract.** A direct-detection Rayleigh-Mie Doppler lidar for measuring horizontal wind speed in the middle atmosphere has been deployed at Observatoire de Haute Provence (OHP) in southern France since 1993. After a recent upgrade, the instrument gained the capacity of wind profiling between 5 and 75 km altitude with high vertical and temporal resolution. The lidar comprises a monomode Nd:Yag laser emitting at 532 nm, three telescope assemblies, and a double-edge Fabry-Perot interferometer for detection of the Doppler shift in the backscattered light. In this article, we describe the instrument design,
15 recap retrieval methodology and provide an updated error estimate for horizontal wind. The evaluation of the wind lidar performance is done using a series of twelve time-coordinated radiosoundings conducted at OHP. A point-by-point intercomparison shows a remarkably small average bias of 0.1 m/s between the lidar and the radiosonde wind profiles with a standard deviation of 2.2 m/s. We report examples of a weekly and an hourly observation series, reflecting various dynamical events in the middle atmosphere, such as a Sudden Stratospheric Warming event in January 2019 and an occurrence of a
20 stationary gravity wave, generated by the flow over the Alps. A qualitative comparison between the wind profiles from the lidar and the ECMWF Integrated Forecast System is also discussed. Finally, we present an example of early validation of the ESA Aeolus space-borne wind lidar using its ground-based predecessor.

1 Introduction

Vertically-resolved measurements of the wind velocity in the middle atmosphere are essential for understanding the
25 global circulation driven by dynamical processes such as gravity and planetary waves interacting with the atmospheric flow (Holton 1983). While weather balloon soundings provide regular observations of horizontal wind profiles up to about 30 km altitude, the region of upper stratosphere and lower mesosphere (USLM, ~30 - 75 km) is poorly covered by observations. The only information on the wind field in this layer available on the regular basis is inferred from horizontal pressure gradients derived from space-borne temperature measurements using geostrophic balance assumption, however this does not allow
30 characterizing regional-scale dynamical processes.



Of particular challenge are the wind measurements in the so-called radar gap between 20 – 60 km (Baumgarten, 2010). Until the early 1990s, the only source of wind measurements in USLM region were the rocket soundings, on which the middle atmosphere wind field climatology was based (Schmidlin, 1986). The high cost of rocket operations has fostered development of remote sensing techniques for wind profiling of the middle atmosphere. Pioneering work in the remote sensing of wind profiles up to the stratopause was conducted by Chanin et al. (1989) at Observatoire de Haute Provence (OHP, 43.9°N, 5.7°E) using incoherent Doppler Rayleigh lidar. Since then, several methods for lidar measurements of wind using molecular backscattering have been proposed and demonstrated (Bills et al., 1991; Abreu et al., 1992; Tepley et al., 1994; Rees et al., 1996; Friedman et al., 1997; Gentry et al., 2000; Yan et al., 2017). A relatively recent development is the Doppler microwave radiometry capable of USLM wind profiling, although with a coarse vertical resolution of ~10 km (Rüfenacht et al., 2012).

While the necessity of high resolution (<1 km) wind profiling of USLM region is well recognized (e.g. Meriwether and Gerrard, 2004; Dörnbrack et al., 2017), there exists presently very few instruments with such capacity which are operated on a regular or quasi-regular basis. These are Doppler lidar at ALOMAR observatory in northern Norway (Baumgarten, 2010; Hildebrand et al., 2017), LiWind lidar at high-altitude Mado observatory at La Reunion island (Baray et al., 2014) and LIOvent lidar at Observatoire de Haute Provence (OHP), where the pioneering lidar measurements of wind up to 50 km altitude were conducted by Chanin et al. (1989).

The OHP wind lidar was originally designed to cover the height range of 25 – 50 km (Garnier and Chanin, 1992), i.e. where the contribution of Mie scattering by aerosol particles can be neglected in most cases. After the eruption of Pinatubo volcano in 1991 polluting the stratosphere with aerosol up to 35 km, the OHP wind lidar was redesigned to minimize the effect of Mie scattering (Souprayen et al., 1999a,b). The new Rayleigh-Mie Doppler lidar named LIOvent was deployed at OHP in late 1993 and was operated on a regular basis during 1995 – 1999. The observations were used for retrieval of gravity wave parameters and stratospheric wind climatology at OHP (Souprayen et al., 1999a; Hertzog et al., 2001) as well as for a study of the effect of gravity waves on ozone fluctuation in the lower stratosphere (Gibson-Wilde et al., 1997).

After a long period of sporadic operation and limited maintenance, the upgrade of OHP wind lidar was started in 2012. At the same time, a similar wind lidar instrument was deployed at Mado observatory at La Reunion island and passed a thorough performance evaluation, which will be presented in a companion paper. The upgrade of both wind lidars included replacement of the laser, optical filtering elements, and detectors. These efforts were largely motivated by the preparation of European Space Agency (ESA) Aeolus satellite mission carrying Doppler wind lidar based on the same principle of Doppler shift detection, i.e. double-edge Fabry-Perot interferometer.

This study aims at characterizing the performance and capacities of OHP LIOvent Doppler lidar after its upgrade. Chapter 2 describes the instrument design; Chapter 3 reports the results of LIOvent validation using 12 collocated radiosoundings; Chapter 4 provides examples of weekly and hourly observation series; Chapter 5 presents an early case of Aeolus validation using OHP lidar; Chapter 6 concludes the study and sketches the outlook.



2 Measurement principle and instrument design

65 A detailed description of the OHP Doppler lidar (LIOvent) and the methodology for retrieving wind profiles was provided by Souprayen et al. (1999a). Here, we recap the measurement principle, the general design of the instrument and its sub-systems, the error budget as well as the principal stages of data retrieval.

2.1 Doppler shift detection

70 The detection of Doppler shift corresponding to the projection of the horizontal wind velocity onto the line-of-sight of the laser (inclined 41° off-zenith) is done using a double-edge Fabry-Perot interferometer (FPI). The FPI, assembled by molecular contact, has two half-disc areas with slightly different air gaps, which results in two distinct bandpasses with a FWHM of 2.03 pm and spectral spacing of 5.24 pm, corresponding to relative difference between the air-gap thicknesses of 10^{-5} . The interferometer is set in a sealed pressure-controlled chamber, allowing a spectral tuning of the FPI bandpasses on both sides of the Rayleigh-Mie backscattered line, whose spectral width varies between about 2 and 2.4 pm depending on atmospheric temperature. The uncertainty in the FPI characteristics induces an uncertainty of $\pm 0.3\%$ on the horizontal wind velocity, whereas the effect of temperature uncertainties does not exceed 0.07% per Kelvin (Souprayen et al., 1999a). The spectral configuration of FPI is conceived to minimize the effect of Mie backscattering (Souprayen et al., 1999b, see Sect. 3.1 for further detail).

80 The spectral tuning of the FPI bandpasses is verified at the beginning of each measurement session through adjustment of the air pressure (i.e. adaptation of the air-gap refractive index) inside the FPI chamber using a stepper motor. The temperature inside the FPI housing module is maintained at 30 C at all times and we note that over many months of lidar operation, the spectral tuning remains stable, except after an occasional laser maintenance.

During a measurement session, the backscattered light is acquired successively from the zenith, north and east lines of sight. The Doppler shift response profile $R(z, \theta)$ for a given line of sight is calculated as:

$$85 \quad R(z, \theta) = \frac{CN_A(z, \theta) - N_B(z, \theta)}{CN_A(z, \theta) + N_B(z, \theta)}, \quad (1)$$

where $N_A(z, \theta)$ and $N_B(z, \theta)$ are the number of photons received from altitude z and transmitted through the bandpasses A and B respectively; and C is the corrective factor accounting for a possible imbalance between the signals in channels A and B due to a difference in detectors' sensitivity. One then deduces the line-position profile (in units of pm) from the response profile through the instrumental calibration function, which accounts for atmospheric temperature profile (Souprayen et al., 1999a).

90 The horizontal wind components are then obtained by subtracting the line-position profile for the vertical pointing $\overline{P}(z, 0^\circ)$, from those of the tilted pointings $P(z, 40^\circ)$:

$$(2) \quad v_h(z) = \frac{c}{2\lambda_0 \sin 40^\circ} [P(z, 40^\circ) - \overline{P}(z, 0^\circ)],$$



95 where λ_0 is the emitted wavelength; and $\overline{P(z, 0^\circ)}$ is the reference (null Doppler-shift) position given by an average in the altitude range of 15–25 km, a region where the vertical wind velocity is negligibly small.

An absolute measurement of wind velocity requires a careful determination of the null Doppler-shift reference. In order to account for the possible drift in the emitted wavelength, typically of 0.03–0.08 pmh⁻¹, the reference measurement is done through 1-minute zenith-pointing acquisition within each 5-minute cycle.

100 2.2 Instrument design and data processing

The transmitter of the lidar is based on a Quanta-Ray Pro290 Q-switched, injection-seeded Nd:YAG laser emitting at 532 nm with a repetition rate of 30 Hz and 800 mJ per pulse energy. The general design of transmitter-receiver system is shown in Fig. 1. The laser beam is commuted successively to the three fixed telescope assemblies, respectively zenith (1), North (2) and East (3) telescopes using a galvanometric scanner mirror (4). Each telescope assembly is comprised of a central transmitter shaft with a beam expander (5) and four collecting parabolic mirrors of 500 mm diameter (6), which translates to
105 the total collective area for each telescope of 0.78 m².

The backscattered light is collected by means of multimode optical fibers located at the focal point of each mirror and linked to an optical commutation chamber (7), which transfers the collected light from a given telescope to the entrance of the spectral analysis sub-system. The latter (not shown) comprises a mode scrambler for homogenizing the incidence angles of
110 light projected onto FPI, a 0.3 nm interference filter for reducing the sky background, and the FPI in a thermally-stabilized pressure-controlled chamber.

The detection of the spectrally-processed light is done with two pairs of cooled Hamamatsu R9880-110 photomultipliers (PMTs), receiving respectively 95% and 5% of the flux (high- and low-gain channels). The high-gain PMTs are electronically gated at 100 μ s, i.e. 15 km radial distance. The acquisition is done using a four-channel Licel transient recorder featuring
115 32760 gates of 50 ns width (i.e. 7.5 m radial resolution).

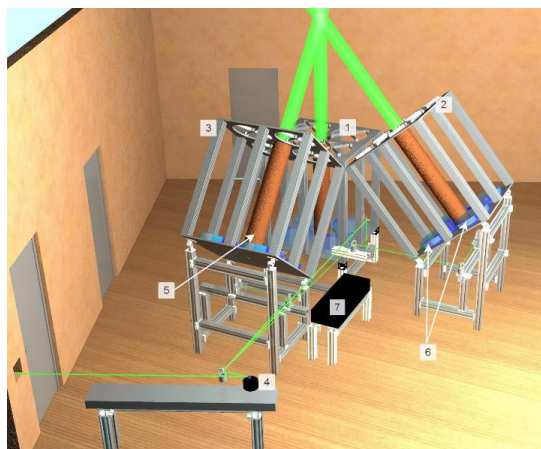
The measurement cadence is such that the zenith, north and east lines of sight are alternated in a cycle of 1–2–2 minutes respectively. A typical acquisition lasts 5 hours during nighttime, that is 2 h integration for each tilted pointing, which ensures signal-to-noise ratio better than 2 all the way up to about 80 km altitude a.s.l. Figure 2a shows an example of raw lidar return profile from the North pointing obtained by stitching the low- and high-gain signals. The vertical range of the useful signal
120 spans between about 5 and 80 km. The lower boundary is due to strong returns from the lower troposphere saturating the detectors in addition to an incomplete geometrical overlap below 2 km.

The photons received from the transient recorder are aggregated over 1-minute intervals and downsampled to 1 μ s bins (150 m radial resolution). The off-line signal pre-processing includes subtraction of background due to sky light and PMT thermal noise as well as dead-time correction, after which the response profiles are calculated for each line-of-sight according
125 to Eq. (1). Then, the Doppler shift (line-position profile) is computed using the instrument calibration function with account



for atmospheric temperature profile, provided by operational analysis by European Center for Medium-range Weather Forecast (ECMWF). Finally, the zonal and meridional wind components are obtained by comparing the tilted East and North pointings to the corresponding zenith pointing using Eq. (2).

130



135

140

Figure 1. Three-dimensional representation of the transmitter-receiver system of LIOvent lidar comprising three telescope assemblies for zenith (1), north (2) and east (3) lines-of-sight with four collecting mirrors (6) and a beam expander (5) each. The emitted laser beam is commuted between the telescopes using rotating scanner mirror (4). The backscattered light collected by each mirror is transferred via fibers into the optical commutation chamber (7) for aggregating the fluxes from the four mirrors of each telescope assembly.

145

2.3 Vertical resolution and statistical uncertainty

Statistical error due to Poisson noise (shot error) increases with altitude proportionally to the exponential decay of molecular backscatter. This is why we use a height-dependent vertical resolution, which is set to 115 m (150 m radial) below 25 km and then increased quasi-exponentially with altitude, from 500 m at 40 km to 4000 m at 70 km (Fig.2b). For a given vertical resolution, we compute the statistical error of an individual response profile:

150

$$\sigma_R = 2C \frac{\sqrt{N_A(N_B - F_{CB})^2 + N_B(N_A - F_{CA})^2}}{[C(N_A - F_{CA}) + (N_B - F_{CB})]^2}, \quad (3)$$

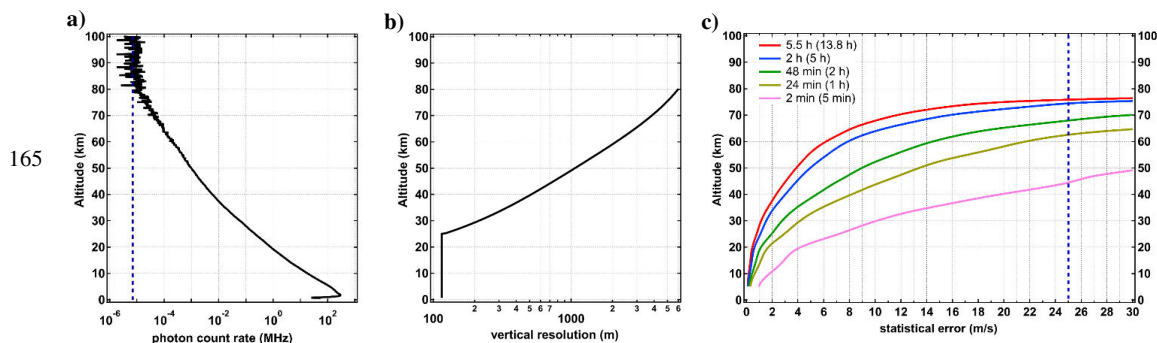
where F_{CA} and F_{CB} is the background signals in channels A and B .

Figure 2c shows the altitude profiles of statistical error for different integration times. For a typical lidar acquisition lasting 5 hours (i.e. 2 hours of a given tilted pointing acquisition, blue curve), the statistical error is less than 2 m/s below 33 km and does not exceed 6 m/s throughout the stratosphere. In the mesosphere, the error increases from 6 m/s at 55 km to 16 m/s at 70 km. A longer acquisition (13.8 h, red curve) reduces the error yet does not extend the vertical coverage: at 75 km altitude, the statistical error for 5 h and 13.8 h acquisition are nearly the same. We use the statistical error value of 25 m/s as a

155



threshold for cut-off altitude of retrieved wind profiles. Given such threshold, the top of vertical range for a standard (5 h) lidar acquisition is ~75 km, whereas a 5-minute acquisition (pink curve), corresponding to a single north-east-zenith measurement cycle, enables coverage up to about 44 km.



165
170

Figure 2. (a): nightly-average raw signal vertical profile obtained in a 7-hour lidar acquisition on 28.01.2019. Dashed blue curve indicates the noise level. (b) altitude-variable vertical resolution used in the retrieval. (c) statistical error profiles computed for different acquisition times of a tilted (north) pointing. The values in brackets correspond to the total duration of lidar acquisition, including zenith, north and east pointings in cycle of 1-2-2 minutes. The dashed blue line marks the cut-off error threshold.

175 3 Comparison with collocated radiosoundings

Over the 4-yr period, spanning June 2015 to June 2019, the validation of the LIOvent wind lidar was conducted using 12 radiosonde (RS) ascents performed at OHP during the time of lidar acquisition. We used Meteomodem M10 radiosondes equipped with GNSS receiver, launched under TOTEX 1200 gr weather balloons. The balloons were reaching on average 29.9 km altitude, whereas the horizontal drift during ascent did not exceed 90 km from the launch point.

180 Figure 3 displays the altitude-coded trajectories of the 12 radiosonde ascents as well as the ground projections of LIOvent tilted pointings. The horizontal displacement of the radiosondes with respect to the lidar sampling location at every altitude level was calculated separately for the East and North pointings and amounted respectively to 27 ± 19.5 km and 39 ± 25 km (1σ), the largest being 117 km for the North pointing. Generally, the displacement increased with altitude as the balloons were drifting away from the lidar sampling locations, as Fig. 3 suggests.

185

190



195

200

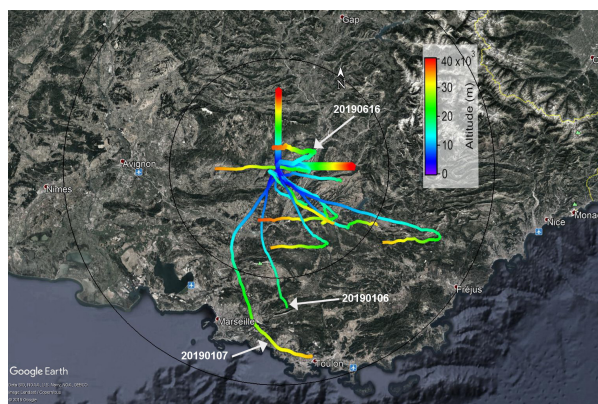


Figure 3. OHP wind lidar sampling location along north and east lines-of-sight (thick lines) and trajectories of 12 radiosondes launched from OHP for wind lidar validation (thinner curves) color-coded by the altitude a.s.l. Black circles indicate the distance from OHP. Particular radiosonde flights are tagged by white arrows with indication of the flight date.

205

For setting up the intercomparison, lidar measurements were averaged over the time period of radiosonde ascent (110 minutes from the ground to 33 km altitude at 5 m/s ascent rate), whereas the radiosonde measurements, reported at 1 Hz frequency, were downsampled to match the vertical resolution of lidar profiles (115 m – 320 m depending on the altitude). The results of intercomparison are reported in Table 1 as absolute difference between RS and LIOvent wind profiles, standard deviation of the differences and correlation for each particular sounding and both wind components.

210

Figure 4 (top panels) shows altitude profiles of the absolute difference between LIOvent and RS for each sounding as well as the mean profile, computed by weighting each difference value by horizontal offset between the measurements. The differences rarely exceed 5 m/s and amount on average to +0.1 m/s and -0.1 m/s respectively for zonal and meridional wind components. While the mean difference profiles do not indicate any altitude-dependent bias, the scatter of differences appears to increase with altitude. This is due, on one hand, to larger horizontal offset between measurements at higher altitudes and, on the other hand, due to increase of statistical error with altitude.

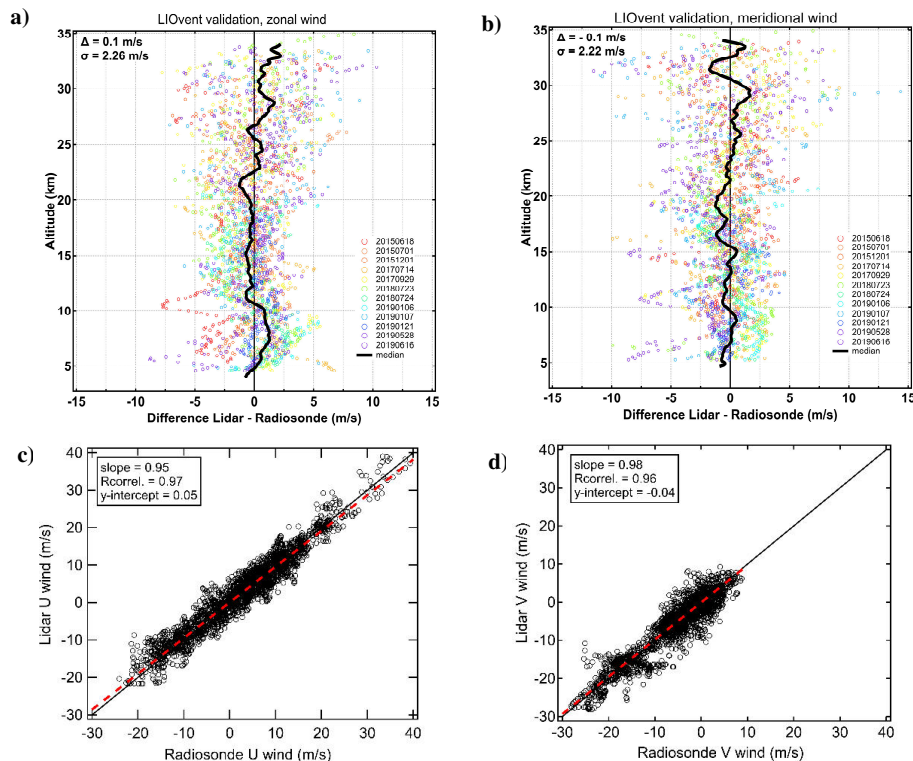
215

The bottom panels of Fig. 4 display the scatter plots of the wind velocities measured by the lidar and the radiosondes with associated regressions and correlation coefficients. For the both wind components, the slope of the regression line is close to 1, which affirms the credibility of the FPI calibration function relating the Doppler shift response to wind velocity. The Pearson correlation coefficient deduced from the ensemble of collocated measurements amounted to 0.97 and 0.96 respectively for zonal and meridional wind velocities.

220



225



230

235

240

245

250

Figure 4. Summary of LIOvent lidar validation using radiosonde ascents from OHP. Top panels: absolute difference between LIOvent and radiosonde zonal (a) and meridional (b) wind velocity for each sounding (date-colored circles, dates provided in the legend) and median profile (black curve), computed by weighting each difference value by horizontal offset between the measurements. The mean difference Δ and the mean standard deviation of the difference (σ) are indicated in the top-left corner of a) and b) panels. Bottom panels: scatter plots of the zonal (c) and meridional (d) wind velocities measured by the lidar and the radiosondes. The 1:1 line is shown in solid black, the linear regression line is shown in dashed red.

The mean standard deviation of the differences for the 12 collocated soundings amounts to 2.26 m/s for the zonal and 2.22 m/s for the meridional wind profiles. These values are consistent with the estimated shot error for a 2 hours lidar acquisition (i.e. duration of a radiosounding), which increases from 0.2 m/s to 3.4 m/s in the altitude range of lidar-radiosonde intercomparison (cf. Fig. 2c). We note that the horizontal-offset weighting of the differences neither affects the mean difference nor the mean correlation but reduces the standard deviation by about 0.2 m/s on average, which suggests that horizontal variability of the wind field on a scale of few tens of kilometres is small.

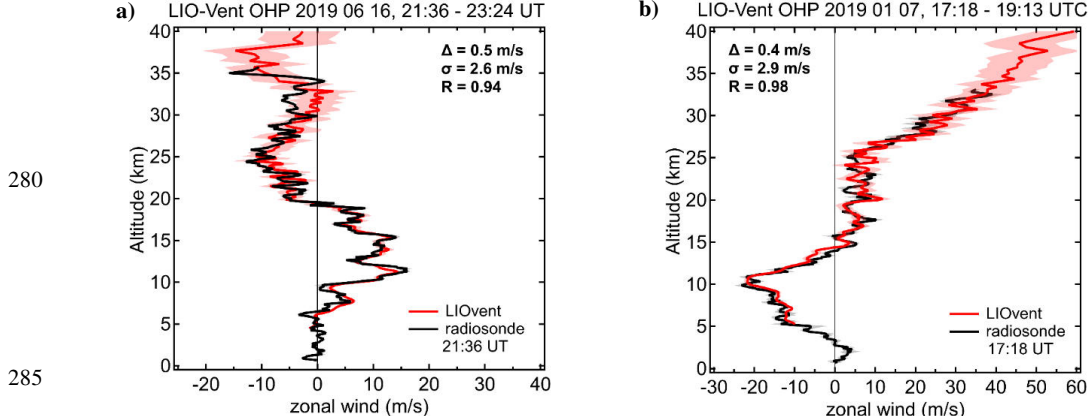


Figure 5 presents examples of summer and winter zonal wind intercomparison cases, both showing directional wind shear in the lower stratosphere but of opposite sign. Remarkably, the small-scale fluctuations, presumably caused by gravity waves propagation and/or breaking, are reproduced by the lidar just as accurately as measured by the balloon sonde, carried by those winds.

At higher altitudes, the fine-scale fluctuations resolved by the lidar appear at times out of phase with those seen by the radiosonde. This is more prominent in the Summer case (Fig. 5a) despite the closer collocation of the measurements. In this case, the RS ascent closely follows the lidar's line-of-sight up until 19 km (cf. Fig. 3) while the LIOvent zonal profile precisely tracks the one of RS up to about the same level. At 19 km, the zonal wind reverses, the balloon makes a U-turn and progressively drifts westward and away from the lidar. Above 30 km, the RS and LIOvent profiles start to get out of phase whilst both showing an increasing easterly wind between 30 – 35 km. The lidar profile, extending above the top of radiosounding, reveals a typical signature of a gravity wave, supposedly propagating in the zonal direction (considering a relatively unperturbed meridional wind profile in this layer, not shown).

While the statistical error of the lidar measurement becomes comparable to the observed variations at these levels, the dephasing of LIOvent and RS profiles in Fig. 5a is likely due to spatially-offset sampling of the gravity wave front. Interestingly, the dephasing above 30 km is less obvious in the winter case (Fig. 5b) despite a considerably larger spatial offset, compared to the summer case (88 km vs 36 km). This may be explained in consideration of the much stronger zonal wind in the winter case (38 m/s versus -2 m/s), damping the amplitude of the wave-induced perturbations.

275



280

285

Figure 5. Selected cases of the lidar-radiosonde intercomparison of the zonal wind profiles in June (a) and January (b) 2019. The lidar measurement dates and times are given above the panels, the time of radiosonde launch on the same date is provided in the legend.

290



3.1 Sensitivity to Mie scattering

A thorough study on the effect of Mie scattering on the wind measurement using the double-edge Fabry-Perot interferometer of the OHP wind lidar was carried out by Souprayen et al. (1999b). Using a theoretical model for the FPI, they recovered the true spectral properties of the interferometer and estimated the particle-induced error for varying values of scattering ratio. They found that for observable stratospheric wind velocities, the residual Mie-induced error is less than 1 m/s for the scattering ratio $R=10$, which is characteristic of a cirrus cloud readily visible to an unaided eye.

Since that time, the interferometer's plates have been subjected to a reconditioning whilst maintaining the desired FPI spectral properties. Nonetheless we have revisited the aspect of FPI sensitivity to particulate scattering. The eruption of the Raikoke stratovolcano (22 June 2019, Kuril Islands, 48° N, 153° E) has polluted the lower stratosphere with a large amount of sulfuric aerosol (NASA EarthObservatory, 2019). The aerosol plumes were observed by OHP lidars every night since 10 July 2019 (and at the time of writing) between 12 and 20 km altitude, which provided an opportunity for testing the sensitivity of wind lidar to Mie-scattering in the stratosphere.

Figure 6 displays lidar measurements of aerosol scattering ratio (SR) and zonal wind velocity on 20 July. The SR profiles were obtained from an aerosol channel (532 nm) of LTA lidar (Keckhut et al., 1993) and from the zenith acquisition of LIOvent lidar using aerosol retrieval method described by Khaykin et al. (2017 and references therein). The LIOvent operation was started after the end of LTA operation since the lidars share the same laser and cannot be operated simultaneously. Both lidars consistently show an aerosol layer at 16.2 km altitude with SR reaching 4.7 and an estimated optical depth of 0.03 which is comparable to a thin cirrus cloud (Hoareau et al., 2013). In addition, the LIOvent measurement reveals a cirrus cloud at 12.2 km, which occurred only towards the end of LTA acquisition and thereby left a weaker imprint in the average SR profile of LTA.

The LIOvent wind measurement in the presence of ice crystals and volcanic aerosol is compared in Fig. 6 to a time-collocated radiosoundings conducted from Nimes airport, located ~100 km west from OHP (cf. Fig. 3). While the vertical structures in the LIOvent and RS wind profiles are at times out of phase (which may be explained by spatial variability), the lidar profile does not show any indications of Mie-induced bias, neither due to a thin cirrus cloud nor due to a volcanic aerosol layer. This result confirms that the spectral configuration of the FPI allows accurate wind measurements in the presence of particles in the middle atmosphere.

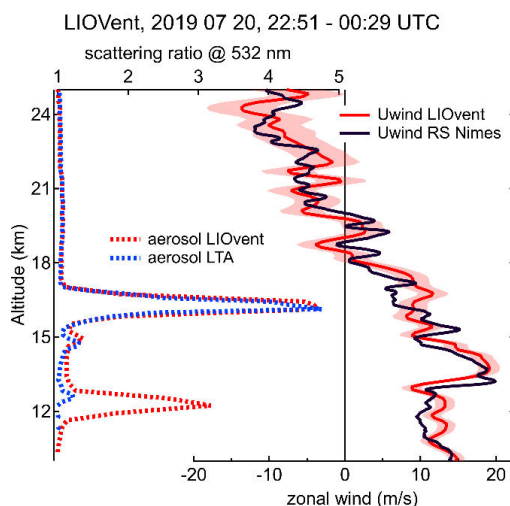
320



325

330

335



340

Figure 6. Zonal wind profiles (bottom axis) measured by the LIOvent wind lidar (red solid) and by MeteoFrance routine radiosounding launched from Nimes airport (100 km away from OHP, see Fig. 3) at 00 UT on 21.07.2019 (black solid). The date and time of LIOvent measurement is shown at the panel top. The aerosol scattering ratio profiles obtained using LIOvent zenith pointing (red dashed) and LTA lidar (blue dashed), showing volcanic aerosol layer at 16.2 km are plotted versus top axis. See text for details.

4 Observations

During the 2015-2019 period, the LIOvent instrument was operated on 52 nights, mostly during early summer and winter seasons. This section reports examples of successive nightly-mean profiles reflecting the wind variability in the middle atmosphere during opposite seasons as well as a particular case of temporally-resolved wind profiling.

345

4.1 January 2019 series

An interesting dynamical event in the USLM was observed in January 2019 during an intensive measurement campaign dedicated to Aeolus validation (AboVE-OHP, Aeolus Validation Experiment at OHP). A strong perturbation of the Arctic circumpolar vortex has occurred as a result of a major Sudden Stratospheric Warming event during the first week of January 2019. According to potential vorticity maps (not shown) based on ECMWF Integrated Forecast System (IFS), the vortex started to split around 1st January and evolved into two separate vortices above Europe and Canada by 4th January. The European counterpart was displaced southward and its edge - at 850 K potential temperature level (~50 km) - reached OHP around 6th January, that is when the AboVE-OHP measurement campaign was started.

350



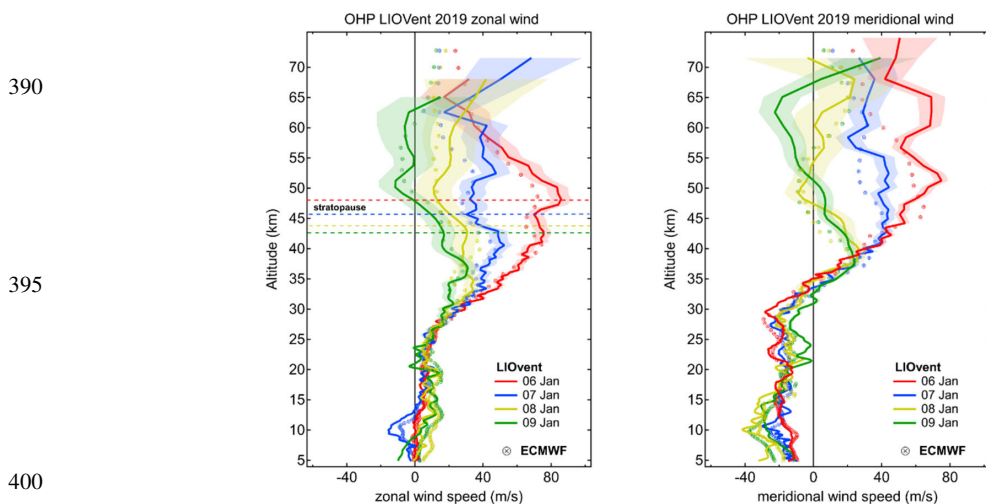
Figure 7 shows ensembles of the zonal and meridional wind profiles obtained during 6 - 9 January period. The plots
355 include indications of the stratopause level which was progressively descending from 47 to 43 km during that period, as
inferred from simultaneous temperature profiling using LiO3S differential absorption lidar (Godin-Beekmann et al., 2003;
Wing et al., 2018). The 6th January wind profiles (red curves) reflect the perturbed conditions when the vortex edge was located
above OHP and both zonal and meridional components were maximizing at 80 m/s around the stratopause. As the edge of
vortex was moving back north of OHP during the following days, the measurements show weakening winds throughout the
360 USLM and reversal of both wind components in the lower mesosphere by 9th January. The rapidly weakening winds form an
envelope of profiles with a bottom at ~27 km for the zonal wind and ~38 km for the meridional component. Below this
envelope, neither of the wind components show significant change over the 4-day period.

The observed evolution of wind profiles is reproduced by the ECMWF T1279/L137 operational analysis represented
by cross-circles in Fig 7. The wind change envelope and the vertical structure of the wind profiles are both well resolved by
365 the model. The ECMWF profiles reproduce the observed vertical fluctuations on a scale of a few kilometres up to the
stratopause, which is remarkable since the regular radiosoundings assimilated into the model hardly reach 30 km altitude. We
note that the consistency between ECMWF and LIOvent is better for the zonal wind, whereas the vertical structures in
meridional wind are somewhat less consistent with the observations in the USLM. Analogous results, inferred from
intercomparison between ALOMAR wind lidar and ECMWF forecast winds, were reported by Rüfenacht et al. (2018). The
370 damping and dephasing of the vertical structures by ECMWF becomes more prominent above about 50 km, which might owe
to both the temporal averaging over 5-13 hours by the lidar and the coarse model resolution in the mesosphere. A detailed
comparison between wind lidar observations, ECMWF IFS and reanalysis data will be the subject of a separate study.

4.2 May 2019 series

Figure 8 shows a sequence of wind profiles acquired during late May 2019. While the winds appear highly variable in
375 the upper troposphere due to the dynamics of the jet stream, the middle stratosphere remains relatively calm and stable over
the considered 4-day period. The zonal wind reverses at around 36 km and the easterlies pick up until ~65 km, that is when
the wind shear reverses. The meridional wind is very weak throughout the stratosphere except for a small envelope at 30 km,
which accompanies the zonal wind perturbations in this layer. The ECMWF IFS accurately resolves this envelope, however
380 the observed vertical structures above, in the USLM, are not reproduced by the model. In particular, the reversal of wind shear
at around 65 km in both wind components is missed by the model, whereas the lidar profiles consistently report this feature,
significant at the permitted statistical error of 25 m/s.

The imposed error threshold of 25 m/s determines the cut-off altitude of the wind profiles reported in Figures 7 and 8.
The top altitude varies between 65 and 75 km depending on the presence of cirrus clouds inhibiting the return signal from
385 above. We note that the meridional profiles normally reach higher altitudes, which is due to a better condition of the collecting
mirrors of the north-pointing telescope assembly.



390

395

400

Figure 7. Ensembles of nightly-mean vertical profiles of zonal (left) and meridional (right) wind profiles obtained by LIOvent in January 2019 (solid curves) with statistical uncertainty shown as shading and the corresponding ECMWF Integrated Forecast System profiles (cross-circles). Horizontal dashed lines in the left panel indicate the stratopause altitude obtained from simultaneous temperature lidar measurements.

405

410

415

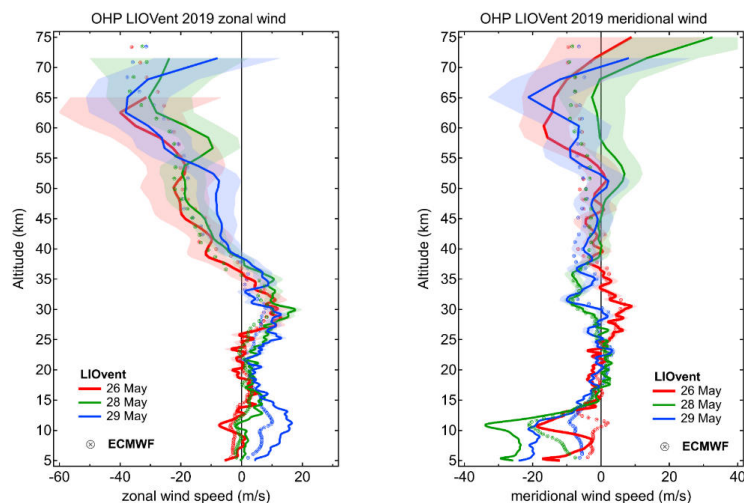


Figure 8. Same as Fig. 7 but for May 2019

420



4.3 Time-resolved wind profiling

An important advantage of the Doppler lidar technique is the capacity to provide temporally-resolved vertical profiling of the atmosphere, which enables characterization of high-frequency fluctuations in the wind profile, inaccessible with snapshot-like radiosonde measurements. Figure 9a provides an example of meridional wind profile variation over the course of a continuous whole-night lidar acquisition lasting nearly 14 hours. Superimposed onto the lidar time-altitude section is a radiosonde ascent, plotted using the same color map as the lidar wind curtain.

The LIOvent and RS profiles are remarkably consistent as can be seen from the color map (correlation coefficient amounts to 0.99 in this case). With that, the lidar wind curtain shows important variation of the wind velocity over the course of 14-hour acquisition. The peak-to-peak variation at any level below 30 km altitude is between 10 and 20 m/s, increasing to ~30 m/s towards 40 km. The wind change rate in any 3 km thick layer is reaching 10 m/s per hour, which points to the predominance of temporal variability of the wind field over its spatial variability. Indeed, the maximum deviation of the lidar profile from the RS one in this case did not exceed 4 m/s at any given level, all the while that the RS measurements were taken as far as 71 km away from the lidar sampling location (cf. Fig. 3).

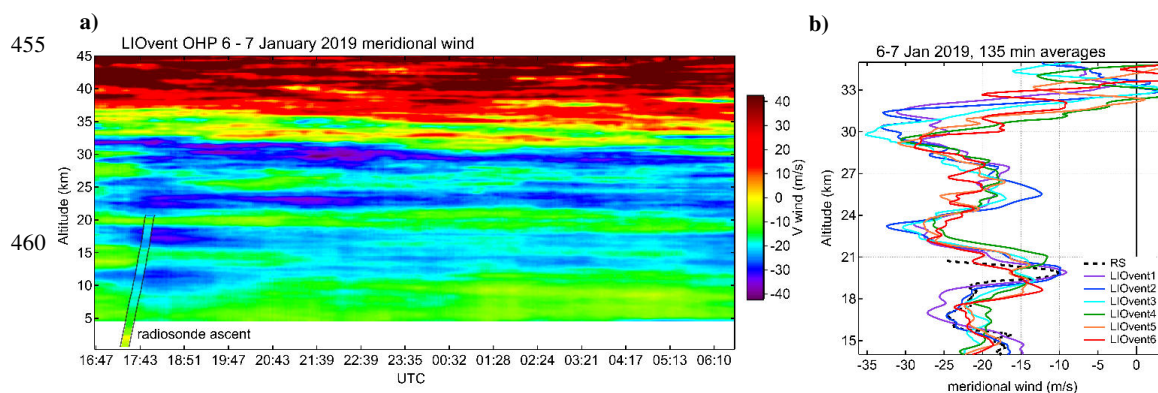
In the upper-middle stratosphere (i.e. around 35 km), where the meridional wind reverses, one can discern wind patterns slowly propagating downward. This pattern is a typical signature of upward-propagating gravity waves with a non-zero ground-based phase speed. A somewhat different pattern is observed in the lower-middle stratosphere (15 – 30 km), where the vertical structures appear to remain constant with altitude. Figure 9b provides a deeper insight into the variable structure of this layer by showing a sequence of 6 wind profiles, obtained by integrating over successive 135-minute temporal intervals as well as the corresponding RS profile. One can see three layers of stronger southward wind at around 17 km, 23 km and 30 km altitude interleaved by two layers of weaker wind at around 20 and 26 km.

The persistence of the observed structures in both temporal and vertical dimensions suggests the occurrence of stationary gravity waves, most likely generated by the flow over the Alpine mountains. Indeed, the circulation in the lower troposphere at that time (not shown) was such that the OHP site was downwind of the Alps. The stationary gravity waves, generated by the flow over the mountain range, could propagate freely into the stratosphere because of the absence of directional wind shear all the way up to 35 km. The amplitude of these wave-induced perturbations appears to increase with altitude from ~5 m/s to ~10 m/s, which is expected from the linear theory of atmospheric waves.

The orographic nature of the gravity wave, identified using time-resolved lidar measurements, can be verified in consideration of the vertical wavelength. For a stationary wave, the vertical wavelength λ_z can be deduced from the horizontal wind speed v_h and the buoyancy frequency N :

$$\lambda_z = 2\pi \frac{v_h}{N} \quad (4)$$

Given the observed $v_h \sim 20$ m/s and $N \sim 0.02$ s⁻¹, we obtain the vertical wavelength of ~6.5 km, which corresponds well to what can be deduced directly from the wind profiles in Fig. 9.



465 **Figure 9.** (a) Temporal variation of the meridional wind profile over the course of a continuous whole-night LIOvent acquisition
started on 6 January 2019. Superimposed onto the lidar time-altitude section is the corresponding radiosonde ascent from OHP,
plotted using the same color map as the lidar wind curtain. (b) successive 135-minute averages of meridional wind measured by the
lidar (solid curves) and the radiosonde profile (black dashed).

5 First results of Aeolus validation

470 Aeolus is the ESA's satellite mission designed to measure wind and aerosol profiles in the troposphere and lower
stratosphere on a global scale (Stoffelen et al., 2005). Launched on 22 August 2018, the Aeolus satellite carries the Atmospheric
LAser Doppler INstrument (ALADIN) which features a telescope of 1.5 m diameter and a laser emitting at 355 nm with a
repetition rate of 50 Hz and ~65 mJ per pulse energy. ALADIN instrument has two detection channels for measuring Doppler
475 shift using the molecular (Rayleigh) and particulate (Mie) backscattering. The Rayleigh channel makes use of a double edge
Fabry-Perot interferometer, that is the measurement principle exploited by the OHP wind lidar.

The ALADIN telescope is pointed 35° away from the orbital plane in order to sense the backscattered light
perpendicular to the trajectory of the satellite. This enables measuring the so-called horizontal line-of-sight (HLOS) wind
velocity, which is close to the zonal wind component except at high latitudes. The Aeolus satellite has a Sun-synchronous
dusk/down orbit with a 7-day repeat cycle, passing near the OHP station (within 100 km) twice per week along the successive
480 ascending and descending orbits, at around 17:50 and 5:50 UT respectively.

As Aeolus and the OHP wind lidar exploit the same measurement technique, the LIOvent instrument is an important
contributor to Aeolus Cal/Val activity. Since January 2019 and by the time of writing, LIOvent has been operated on 27 nights,
providing 8 measurements collocated with Aeolus overpasses. Some of the Aeolus-collocated LIOvent acquisitions were
accompanied by simultaneous radiosonde ascents. While a comprehensive validation exercise will be the subject of a separate
485 study, here we provide an example of comparison between collocated Aeolus L2B02 'Rayleigh-clear' and LIOvent wind



profiles. One should bear in mind that Aeolus wind data processing is still being improved by optimizing the in-orbit instrument calibration, therefore the presented validation case is to be considered as preliminary.

Figure 10 displays a collocation case from 7 January 2019 when the satellite was sampling the atmosphere around 100 km west of OHP along the ascending orbit. The plot includes two successive Aeolus wind profiles (blue dashed) obtained by 12 seconds integration (i.e. 90 km along-track distance) as well as their mean (blue solid). The LIOvent and RS wind components are converted to Aeolus HLOS wind and reported at their native vertical resolution (solid red and black) as well as after downsampling to Aeolus vertical resolution (circles).

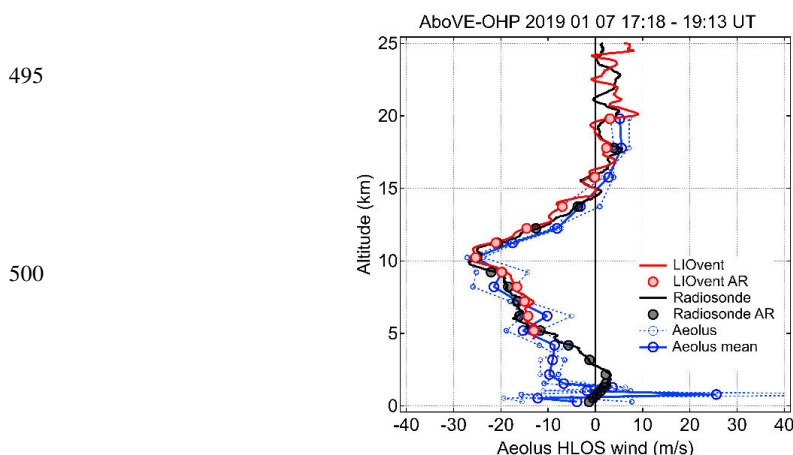


Figure 10. Example of the validation of preliminary L2B HLOS wind of the ESA Aeolus Doppler lidar using the LIOvent lidar and a radiosounding within AboVE-OHP campaign. The LIOvent and RS wind components are converted to Aeolus HLOS wind and reported at their native vertical resolution (solid red and black) as well as after downsampling to Aeolus vertical resolution (circles, marked AR in the legend). The Aeolus overpass near OHP took place at 17:50 UT (ascending orbit). The lidar acquisition time (corresponding to the radiosonde ascent time) is provided in the panel top. See text for further details.

The profiles are found to be in good agreement, consistently reproducing the peak in the eastward wind of -25 m/s at 10 km, which corresponds to an anticyclonic feature of the jet stream (not shown). In the middle troposphere, successive Aeolus profiles appear somewhat scattered around their mean, with the latter being in better agreement with the ground-based measurements. Below 5 km, the Aeolus profile deviates from the RS, which may be caused by a stronger spatial variability of the wind field in the lower troposphere. In the lower stratosphere, that is above about 11 km, Aeolus follows well the downsampled measurements by OHP lidar and radiosonde. The average difference between the mean Aeolus and downsampled LIOvent HLOS wind profiles in the overlapping range of 5 - 20 km amounts in this case to +1.5 m/s with a



standard deviation of 3.2 m/s and a correlation coefficient of 0.96. Similar values were obtained from other collocations during
520 AboVE-OHP campaign in January 2019.

6 Summary and outlook

The OHP wind lidar presented here was a unique instrument at the time of its creation and remains one of the very few
instruments capable of wind profiling in the middle atmosphere with high vertical and temporal resolution. In this paper, we
have described the design of the instrument after its upgrade and evaluated its capacities using a dozen time-located
525 radiosoundings launched from OHP. We have shown that the lidar is capable of measuring horizontal wind velocity between
5 and 75 km altitude with an error of less than 6 m/s up to the top of the stratosphere. We note that the vertical range can
potentially be extended to 3 – 80 km through replacement of certain optical elements, for which the resources are available.

A noticeable result of the lidar-radiosonde intercomparison is a remarkably small average bias of 0.1 m/s for the both
wind components. This finding affirms the reliability of the on-the-run calibration (through periodical zenith pointing) as well
530 as the stability of the FPI calibration function. Also remarkable is that the small-scale wind fluctuations are reproduced by the
lidar just as accurately as measured by the balloon sondes, carried by those winds. The average standard deviation of the
differences was found to be only ~2.2 m/s, which is consistent with the error estimates for the considered altitude range. The
correlation coefficient obtained from the ensemble of collocated measurements amounted to 0.96.

We have shown that wind profiling with the LIOvent lidar is insensitive to the presence of particles (thin cirrus clouds
535 or stratospheric aerosols) and we have demonstrated the capacity of the wind lidar to measure vertical profiles of aerosol
backscattering. In addition, using the 3 different lines-of-sight, one can obtain information on the fine-scale horizontal
variability of stratospheric aerosol.

The examples of successive nightly-mean wind profiles given in Sect. 4.1 and 4.2 provide interesting insight into the
wind variability in the upper stratosphere and lower mesosphere, the atmospheric layer of exceptionally poor observational
540 coverage. The observed vertical structures and the rapidly changing wind shear reflect the complex dynamics of the USLM
layer and its two-way interactions with the upward-propagating gravity waves, whose manifestation may be not well
reproduced by atmospheric models. We note though that ECMWF operational model tends to reproduce, in most cases, the
observed vertical structures at least up to 50 km altitude.

The example of time-resolved wind profiling presented in Sect. 4.3 highlights the capacity of LIOvent instrument to
545 detect high-frequency fluctuations in the wind profile, indicative of various types of gravity waves. This rare capacity enables
a comprehensive characterization of the high-frequency part of the wave spectrum, inaccessible with any other measurement
technique. At OHP, the wind lidar acquisitions are typically accompanied by temperature profiling using Rayleigh lidar, which
altogether provides a complete suite of thermodynamical parameters in the middle atmosphere on a regular basis and on a long
term.



550 Using the time-resolved wind profiling and simultaneous radiosoundings, we have found that the temporal variability of wind profile in the free atmosphere at a scale of 1 hour may be at least twice as large as the spatial variability on a scale of 50-100 km, as deduced from the lidar-radiosonde intercomparison. This finding is to be considered for Aeolus wind validation activities and particularly for the satellite overpass spatial and temporal collocation criteria.

We have presented the first preliminary case of Aeolus validation using the LIOvent lidar. We note that while the
555 Aeolus data processing and calibration may be subject to further improvement, the first results of intercomparison between the ground-based and space-borne Doppler lidars are encouraging. The validation of Aeolus is to be continued at OHP on a regular basis for monitoring of the long-term stability of the satellite lidar, whereas a dedicated Aeolus validation study will be conducted in a separate article.

Further studies exploiting LIOvent observations will address the characteristics of gravity waves retrieved from
560 simultaneous wind and temperature profiling at OHP as well as intercomparison with operational analysis and new reanalysis data sets such as ECMWF ERA5. The lidar wind profiling is also to be used in conjunction with infrasound measurements carried out at OHP (Le Pichon et al., 2015) for studies of middle atmosphere dynamics.

Data availability. The lidar and radiosonde data are currently available on request. The wind lidar data will be soon
565 made available through the AERIS data portal at <https://cds-espri.ipsl.upmc.fr/NDACC/station?methodName=viewDataOhp>

Authors contributions. SK and AH conceived the study and conducted the LIOvent measurements, RW conducted the LIOvent measurements and extracted Aeolus data, PK offered scientific insight, SGB offered scientific insight and provided access to LiO3S lidar data, JP conceived the optical design of LIOvent instrument, JFM and JS upgraded and optimized the
570 wind lidar. The paper is written by SK with contributions from all co-authors.

Acknowledgements. The upgrade of OHP wind lidar was financially supported by CNES (Centre Nationale des Etudes Spatiales) as well as through EU FP7 ARISE and H2020 ARISE2 projects. We thank the personnel of Station Gerard Megie at OHP, Frederic Gomez, Pierre Da Conceicao, Yohann Pignon and others for conducting the radiosonde launches and lidar
575 operation. We thank Alexis Le Pichon (CEA) for providing ECMWF wind profiles for OHP location and Andreas Dörnbrack (DLR) for providing high-resolution PV polar projections based on ECMWF IFS data. The work related to Aeolus validation has been performed in the frame of Aeolus Scientific Calibration & Validation Team (ACVT) activities. Results are based on preliminary (not fully calibrated/validated) Aeolus data, that have not yet been publically released. Further data quality improvements, including in particular a significant product bias reduction, will be achieved before the public data release.
580 Aeolus is a European Space Agency (ESA) mission from the Earth Explorer Program of research satellites. We thank Anne Grete Straume (Aeolus mission scientist) and Jonas von Bismark (Aeolus data quality manager) for the fruitful exchange on this study,



585

Date	Mean diff., m/s		St. dev, m/s		R correl		Distance, km		Top of RS, km
	U	V	U	V	U	V	U	V	
2015 06 18	-1.3	0.1	2.9	2.3	0.95	0.96	31	47	32.5
2015 07 01	0.9	-0.8	2.1	1.2	0.92	0.89	16	21	28.0 ⁵⁹⁰
2015 12 01	-0.4	0.6	1.8	2.0	0.96	0.96	15	27	33.0
2017 07 14	0.1	-0.3	2.6	3.1	0.98	0.79	46	69	33.0
2017 09 29	-0.0	0.65	2.7	2.7	0.93	0.85	18	38	33.0
2018 07 23	0.29	0.1	3.2	2.9	0.97	0.88	21	38	37.3
2018 07 24	0.2	0.0	1.6	1.3	0.99	0.89	8	22	20.1 ⁵⁹⁵
2019 01 06	-0.1	0.9	2.5	2.1	0.9	0.99	37	45	20.9
2019 01 07	0.4	-0.7	2.9	3.8	0.98	0.98	57	67	33.5
2019 01 21	0.1	0.0	0.9	1.5	0.99	0.98	13	20	18.0
2019 05 28	-0.2	-2.0	2.7	3.6	0.94	0.89	27	49	32.5 ⁶⁰⁰
2019 06 16	0.6	-0.5	2.5	2.5	0.94	0.72	12	15	37

605 **Table 1. Summary of intercomparison between LIOvent lidar and time-collocated radiosoundings launched at OHP. The results are shown separately for zonal (U) and meridional (V) wind measurements and include for each case of intercomparison (from left to right): measurement date, mean absolute difference, standard deviation of the differences, correlation coefficient, mean horizontal distance between the lidar and radiosonde sampling locations and top altitude of radiosounding.**

610

615



References

- Abreu, V. J., J. E. Barnes, and P. B. Hays, Observations of winds with an incoherent lidar detector, *Appl. Opt.*, 31, 620 4509-4514, 1992.
- Baray, J.-L., Courcoux, Y., Keckhut, P., Portafaix, T., Tulet, P., Cammas, J.-P., Hauchecorne, A., Godin Beekmann, S., De Mazière, M., Hermans, C., Desmet, F., Sellegri, K., Colomb, A., Ramonet, M., Sciare, J., Vuillemin, C., Hoareau, C., Dionisi, D., Duflot, V., Vérémes, H., Porteneuve, J., Gabarrot, F., Gaudo, T., Metzger, J.-M., Payen, G., Leclair de Bellevue, J., Barthe, C., Posny, F., Ricaud, P., Abchiche, A., and Delmas, R.: Maïdo observatory: a new high-altitude station facility at 625 Reunion Island (21° S, 55° E) for long-term atmospheric remote sensing and in situ measurements, *Atmos. Meas. Tech.*, 6, 2865–2877, <https://doi.org/10.5194/amt-6-2865-2013>, 2013.
- Baumgarten, G.: Doppler Rayleigh/Mie/Raman lidar for wind and temperature measurements in the middle atmosphere up to 80 km, *Atmos. Meas. Tech.*, 3, 1509–1518, <https://doi.org/10.5194/amt-3-1509-2010>, 2010.
- Bills, R. E., C. S. Gardner, and S. J. Franke, Na Doppler/temperature lidar: Initial mesopause region observations and 630 comparison with the Urbana medium-frequency radar, *J. Geophys. Res.*, 96, 22,701-22,707, 1991.
- Chanin, M. L., Garnier, A., Hauchecorne, A., and Porteneuve, J.: A Doppler lidar for measuring winds in the middle atmosphere, *Geophys. Res. Lett.*, 16, 1273–1276, <https://doi.org/10.1029/GL016i01p01273>, 1989.
- Dörnbrack, A., Gisinger, S., and Kaifler, B.: On the interpretation of gravity wave measurements by ground-based lidars, *Atmosphere*, 8, 49, <https://doi.org/10.3390/atmos8030049>, 2017.
- 635 Friedman, J. S., Tepley, C. A., Castleberg, P. A., and Roe, H.: Middle-atmospheric Doppler lidar using an iodine-vapor edge filter, *Opt. Lett.*, 22, 1648–1650, doi:10.1364/OL.22.001648, 1997.
- Garnier A., M. L. Chanin, 1992: Description of a Doppler Rayleigh lidar for measuring winds in the middle atmosphere, *Appl. Phys.*, B, 55, 35-40.
- Gentry, B. M., Chen, H., and Li, S. X.: Wind measurements with 355-nm molecular Doppler lidar, *Opt. Lett.*, 25, 1231– 640 1233, doi:10.1364/OL.25.001231, 2000.
- Gibson-Wilde, D. E., R. A. Vincent, C. Souprayen, S. Godin, A. Hertzog, and S. D. Eckermann, Dual lidar observations of mesoscale fluctuations of ozone and horizontal winds, *Geophys. Res. Lett.*, 24, 1627-1630, 1997.
- Hertzog, A., C. Souprayen and A. Hertzog : Measurements of gravity wave activity in the lower stratosphere by Doppler lidar, *J. Geophys. Res.*, 106, D8, 7879-7890, 2001.
- 645 Hildebrand, J., Baumgarten, G., Fiedler, J., and Lübken, F.-J.: Winds and temperatures of the Arctic middle atmosphere during January measured by Doppler lidar, *Atmos. Chem. Phys.*, 17, 13345–13359, <https://doi.org/10.5194/acp-17-3345-2017>, 2017.
- Hoareau, C., Keckhut, P., Noel, V., Chepfer, H., and Baray, J.-L.: A decadal cirrus clouds climatology from ground-based and spaceborne lidars above the south of France (43.9° N–5.7° E), *Atmos. Chem. Phys.*, 13, 6951-6963, 650 <https://doi.org/10.5194/acp-13-6951-2013>, 2013.



- Holton, J.R., 1983: The Influence of Gravity Wave Breaking on the General Circulation of the Middle Atmosphere. *J. Atmos. Sci.*, 40, 2497–2507, <https://doi.org/10.1175/1520-0469>, 1983.
- Keckhut P., A. Hauchecorne and M. L. Chanin (1993), A critical review on the data base acquired for the long term surveillance of the middle atmosphere by french rayleigh lidars, *J. Atmos. Oceanic Technol.*, 10, 850-867, 1993.
- 655 Khaykin, S. M., Godin-Beekmann, S., Keckhut, P., Hauchecorne, A., Jumelet, J., Vernier, J.-P., Bourassa, A., Degenstein, D. A., Rieger, L. A., Bingen, C., Vanhellemont, F., Robert, C., DeLand, M., and Bhartia, P. K.: Variability and evolution of the midlatitude stratospheric aerosol budget from 22 years of ground-based lidar and satellite observations, *Atmos. Chem. Phys.*, 17, 1829–1845, <https://doi.org/10.5194/acp-17-1829-2017>, 2017.
- 660 Khaykin, S.M., A. Hauchecorne, J.-P. Cammas, N. Marqestaut, J.-F. Mariscal, F. Posny, G. Payen, J. Porteneuve, P. Keckhut. Exploring fine-scale variability of stratospheric wind above the tropical la reunion island using Rayleigh-Mie Doppler lidar. *EPJ Web Conf. Volume 176, The 28th International Laser Radar Conference (ILRC 28)*, <https://doi.org/10.1051/epjconf/201817603004>, 2018
- Le Pichon, A., J. D. Assink, P. Heinrich, E. Blanc, A. Charlton-Perez, C. F. Lee, P. Keckhut, A. Hauchecorne, R. Rüfenacht, N. Kämpfer, D. P. Drob, P. S. M. Smets, L. G. Evers, L. Ceranna, C. Pilger, O. Ross, and C. Claud: Comparison of co-located independent ground-based middle atmospheric wind and temperature measurements with numerical weather prediction models, *J. Geophys. Res. Atmos.*, 120, 8318-8331, [doi:10.1002/2015JD023273](https://doi.org/10.1002/2015JD023273), 2015.
- 665 Meriwether, J. W. and Gerrard, A. J.: Mesosphere inversion layers and stratosphere temperature enhancements, *Rev. Geophys.*, 42, RG3003, <https://doi.org/10.1029/2003RG000133>, 2004.
- NASA Earth Observatory, Raikoke erupts, Retrieved 26 June 2019.
- 670 <https://earthobservatory.nasa.gov/images/145226/raikoke-erupts>
- Rees, D., Vyssogorets, M., Meredith, N. P., Griffin, E., and Chaxell, Y.: The Doppler Wind and Temperature System of the ALOMAR Lidar facility: overview and initial results, *J. Atmos. Sol.-Terr. Phys.*, 58, 1827–1842, [doi:10.1016/0021-9169\(95\)00174-3](https://doi.org/10.1016/0021-9169(95)00174-3), 1996.
- Rüfenacht, R., Kämpfer, N., and Murk, A.: First middle atmospheric zonal wind profile measurements with a new ground-based microwave Doppler-spectro-radiometer, *Atmos. Meas. Tech.*, 5, 2647–2659, <https://doi.org/10.5194/amt-5-2647-2012>, 2012.
- 675 Rüfenacht, R., Baumgarten, G., Hildebrand, J., Schranz, F., Matthias, V., Stober, G., Lübken, F.-J., and Kämpfer, N.: Intercomparison of middle-atmospheric wind in observations and models, *Atmos. Meas. Tech.*, 11, 1971–1987, <https://doi.org/10.5194/amt-11-1971-2018>, 2018.
- 680 Schmidlin, F., Carlson, M., Rees, D., Offermann, D., Philbrick, C., and Widdel, H. U.: Wind structure and variability in the middle atmosphere during the November 1980 Energy Budget Campaign, *J. Atmos. Terr. Phys.*, 47, 183–193, [https://doi.org/10.1016/0021-9169\(85\)90133-3](https://doi.org/10.1016/0021-9169(85)90133-3), 1985.



Souprayen, C., Garnier, A., Hertzog, A., Hauchecorne, A., and Porteneuve, J.: Rayleigh-Mie Doppler wind lidar for atmospheric measurements. Instrumental setup, validation, and first climatological results, *Appl. Opt.*, 38, 2410–2421, 685 <https://doi.org/10.1364/AO.38.002410>, 1999a.

Souprayen, C., Garnier, A., Hertzog, A.: Rayleigh–Mie Doppler wind lidar for atmospheric measurements. II. Mie scattering effect, theory, and calibration, *Appl. Opt.*, 38, 2422–2431, <https://doi.org/10.1364/AO.38.002422>, 1999b.

Tepley, C. A.: Neutral winds of the middle atmosphere observed at Arecibo using a Doppler Rayleigh lidar, *J. Geophys. Res.- Atmos.*, 99, 25781–25790, <https://doi.org/10.1029/94JD02213>, 1994.

690 Wing, R., Hauchecorne, A., Keckhut, P., Godin-Beekmann, S., Khaykin, S., McCullough, E. M., Mariscal, J.-F., and d'Almeida, É.: Lidar temperature series in the middle atmosphere as a reference data set – Part 1: Improved retrievals and a 20-year cross-validation of two co-located French lidars, *Atmos. Meas. Tech.*, 11, 5531–5547, <https://doi.org/10.5194/amt-11-5531-2018>, 2018.

695 Yan, Z., Hu, X., Guo, W., Guo, S., Cheng, Y., Gong, J., and Yue, J.: Development of a mobile Doppler lidar system for wind and temperature measurements at 30–70 km, *J. Quant. Spectrosc. Ra.*, 188, 52–59, <https://doi.org/10.1016/j.jqsrt.2016.04.024>, 2017.